

# Rayburst sampling, an algorithm for automated three-dimensional shape analysis from laser scanning microscopy images

Alfredo Rodriguez<sup>1–3</sup>, Douglas B Ehlenberger<sup>1–3</sup>, Patrick R Hof<sup>1,3</sup> & Susan L Wearne<sup>1–3</sup>

<sup>1</sup>Fishberg Department of Neuroscience, <sup>2</sup>Center for Biomathematical Sciences, <sup>3</sup>Computational Neurobiology and Imaging Center, Mount Sinai School of Medicine, New York, New York 10029, USA. Correspondence should be addressed to S.L.W. (susan.wearne@mssm.edu)

Published online 7 December 2006; doi:10.1038/nprot.2006.313

**Precise quantification of complex three-dimensional (3D) structures from laser scanning microscopy (LSM) images is increasingly necessary in understanding normal function and pathologic processes in biology. This protocol describes a versatile shape analysis algorithm, Rayburst sampling, that generates automated 3D measurements from LSM images. Rayburst defines and efficiently casts a multidirectional core of rays from an interior point to the surface of a solid, allowing precise quantification of anisotropic and irregularly shaped 3D structures. Quantization error owing to the finite voxel representation in digital images is minimized by interpolating intensity values continuously between voxels. The Rayburst algorithm provides a primitive for the development of higher level algorithms that solve specific shape analysis problems. Examples are provided of applications to 3D neuronal morphometry: (i) estimation of diameters in tubular neuronal dendritic branching structures, and (ii) measurement of volumes and surface areas for dendritic spines and spatially complex histopathologic structures.**

## INTRODUCTION

Accurate estimation of diameters, volumes and surface areas of complex 3D structures imaged with LSM requires versatile and efficient techniques. Such morphological parameters are of general interest in many domains of biology and in the study of pathological states. For example, in the case of the central nervous system, understanding the role of structural changes in initiating the functional deficits seen in conditions such as normal brain aging and neuropsychiatric illnesses requires accurate and detailed 3D reconstructions of neuronal morphology, and realistic modeling of neurons' biophysical properties to relate structural changes directly to altered firing patterns<sup>1–8</sup>. These analyses depend on the ability to digitize complex biological structures in 3D with sufficient accuracy and automation for objective and reliable statistics. Traditional 3D methods based on manual tracing tools such as NeuroZoom<sup>9</sup> or NeuroLucida (MicroBrightField) introduce subjective errors and are time consuming to implement. More recently, techniques of varying degrees of automation have been introduced<sup>10–17</sup>. In many cases, however, the limited size of the data sets that can be handled and the general requirement for manual post-processing render these infeasible for the large data sets required to reconstruct entire neurons or multicellular structures at high resolution. In addition, most of these techniques are specialized to a particular class of structures and are not easily generalized to irregular 3D shapes.

The precision of existing image analysis-based morphometric tools is restricted at the finest scales, where resolution of subcellular structures such as detailed spine geometry is limited by quantization errors arising from insufficient imaging resolution. In this protocol, we describe a novel shape analysis technique, the Rayburst sampling algorithm, that uses the original LSM grayscale data rather than segmented images for precise radial and volumetric estimation. The Rayburst sampling algorithm generates a multidirectional set of unit rays called the sampling core, which are cast efficiently from the interior of a volumetric structure to determine the radial distance to the surface of the object in each direction. The

technique interpolates intensity values continuously between voxels, allowing subvoxel resolution of local surfaces and smoothing the quantization artifact in digital images. This greatly improves the resolution of small structures such as neuronal dendritic spines, which may be represented by only a few voxels, even when imaged at the limits of resolution of light microscopy. Surface areas and volumes of 3D objects can then be computed to arbitrary levels of accuracy by integrating over the triangular surface mesh and resulting pyramidal volumetric discretization that are defined by the rays. The number of rays can be varied as a trade-off between accuracy and speed of execution. In many applications, using a two-dimensional (2D) rather than a 3D sampling core can optimize both speed and accuracy by avoiding the optical smear caused by the point spread function of the microscope, hence eliminating the need for lengthy deconvolution processing. We demonstrate how the information returned from 2D and 3D Rayburst sampling can be used to compute local diameters, surface areas and volumes of 3D structures, with specific applications to neuronal dendritic branches, spine morphometry and spatially complex histopathologic lesions.

## The sampling core

The sampling core can be 2D or 3D, with a variable number of rays,  $N$ , depending on the application. Accurate representation of each direction by the sampling core requires that its  $N$  vectors be uniformly spaced over the unit sphere. In the case of a 2D core, this can be accomplished easily by rotating a single ray in the plane at equal angular increments. Generating a 3D core is more complex, and a number of methods could be used depending on the desired results (ref. 18; see also ref. 19). For calculation of surface areas and volumes from Rayburst, it is most efficient to derive the rays from the nodes of a geodesic sphere. This method automatically generates a sequence of increasingly fine triangular meshes that comprise the basis for numerical surface area and volume

calculations. A geodesic sphere can be simply constructed from recursive subdivision of the triangular faces of a regular tetrahedron, octahedron or icosahedron.

We explain this stepwise process in the PROCEDURE, using an octahedron as the basis for our geodesic sphere (Fig. 1).

### Casting rays through the volume

A 3D data set of microscopy images can be viewed as a regular grid of intensity values, each representing a point sample of the data (Fig. 2a), with integer coordinates in a 3D cartesian coordinate system. Each set of eight adjacent values forms a cuboid cell with one intensity value at each vertex (e.g., bottom right cube, Fig. 2a, and zoomed version, Fig. 2b). The intensity value at an arbitrary location inside this cuboid cell can be estimated from the known vertex values using piecewise trilinear interpolation<sup>20</sup>. To cast a ray from an interior point to the surface of a structure, the intensity value at repeated increments along the ray's trajectory must be continuously evaluated to determine when the surface has been reached. For the purpose of specifying the object boundary, a threshold value for intensity is selected. In the case of confocal laser scanning microscopy (CLSM) data, values at or above the threshold are said to be part of the structure whereas those below are part of the background. This threshold value must remain constant throughout the casting of a single core, but may be adjusted at each Rayburst location in cases where many measurements are needed. Currently, we use a dynamically varying threshold to adjust for irregularities in intensity levels in the images. This allows a new threshold to be computed at each node in the dendritic arbor and a new Rayburst run using that locally determined threshold.

Trilinear interpolation can be used to estimate the intensity value at repeated increments along the length of the ray<sup>19</sup>, but this can be slow and requires pre-selection of an arbitrary increment value, with the difficulty of balancing speed and accuracy. Any value greater than the size of a voxel may result in entire voxels being skipped, whereas too small a value will increase computation without significant benefit. Whatever the fixed increment selected, obliquely oriented rays may skip a cell entirely, introducing interpolation artifacts. To avoid these problems, we reduce the

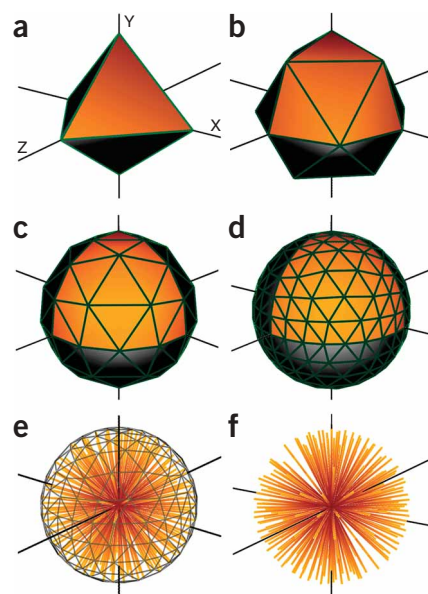


**Figure 1** | Recursive subdivision of a regular octahedron to obtain a geodesic unit sphere from which the Rayburst sampling core, with an associated triangular surface mesh, can be derived. (a) Initial octahedron used to generate sampling core. (b) The orange triangular face in a is subdivided into four new triangles. (c,d) Recursive subdivision of triangular faces. (e) Rayburst core with superimposed geodesic sphere and triangular mesh. (f) Final Rayburst core.

computation to a series of bilinear interpolations by identifying the face of exit for each cell encountered along the trajectory of the ray (yellow faces, Fig. 2a). A face is defined as the rectangular space surrounded by four neighboring voxels. Over this space, the intensity value may be determined using bilinear interpolation of the four surrounding voxels. This simpler method avoids selection of an arbitrary increment and is guaranteed to evaluate every cuboid cell along the trajectory of the ray.

### Computing the face of exit

Consider a ray with components  $[x_r, y_r, z_r]$  and a starting location  $[x_0, y_0, z_0]$  inside the cuboid cell highlighted in Figure 2b. For a particular ray, the face of exit is given by one of the following plane equations:  $x = i$ , for a YZ plane displaced  $i$  units along the X axis;  $y = j$ , for an XZ plane displaced  $j$  units along the Y axis; or  $z = k$ , for an XY plane displaced  $k$  units along the Z axis, where

$$i = \text{ceil}(x_0 - 1), \text{ if } x_r < 0 \quad \text{or} \quad \text{floor}(x_0 + 1), \text{ if } x_r \geq 0 \quad (1)$$

$$j = \text{ceil}(y_0 - 1), \text{ if } y_r < 0 \quad \text{or} \quad \text{floor}(y_0 + 1), \text{ if } y_r \geq 0 \quad (2)$$

$$k = \text{ceil}(z_0 - 1), \text{ if } z_r < 0 \quad \text{or} \quad \text{floor}(z_0 + 1), \text{ if } z_r \geq 0. \quad (3)$$

The functions **ceil()** and **floor()** round to the nearest larger or smaller integer, respectively, depending on the sign of the specified ray component. To determine the correct face of exit, we parametrize the ray as

$$x = x_0 + tx_r, \quad 0 < t < \infty \quad (4)$$

$$y = y_0 + ty_r, \quad 0 < t < \infty \quad (5)$$

$$z = z_0 + tz_r, \quad 0 < t < \infty. \quad (6)$$

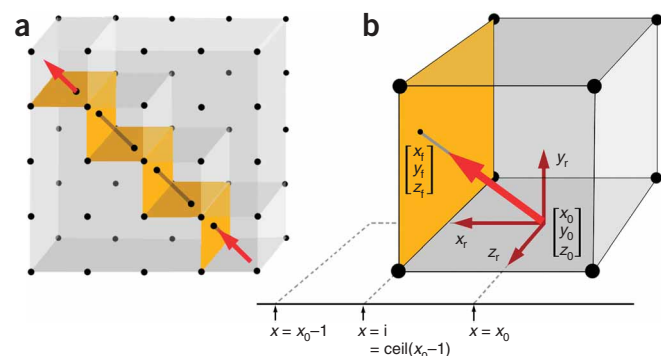


**Figure 2** | Iterative computation of face of exit of a ray. (a) 3D grid of sampled intensity values representing digitized microscopy image stacks. Each point is a voxel. Red arrows show start and end of a single ray that is cast iteratively through the yellow cuboid faces (black trajectory). (b) Zoomed view of bottom right cube in a. Large red arrow indicates the ray,  $r$ , with components  $[x_r, y_r, z_r]$  given by thin red arrows and origin  $[x_0, y_0, z_0]$ . Yellow face of exit is the plane  $x = i$ . The ray crosses the face of exit at  $[x_f, y_f, z_f]$ .

## PROTOCOL

The ray crosses the planes given by expressions (1), (2) and (3) at values of  $t$  given by

$$t_x = (i - x_0)/x_r \quad \text{for the plane } x = i \quad (7)$$

$$t_y = (j - y_0)/y_r \quad \text{for the plane } y = j \quad (8)$$

$$t_z = (k - z_0)/z_r \quad \text{for the plane } z = k. \quad (9)$$

The minimum of  $\{t_x, t_y, t_z\}$ ,  $t_{\min}$ , specifies the face of exit, and the coordinates of the exit location,  $[x_f, y_f, z_f]$ , can be determined by substituting  $t = t_{\min}$  into equations (4–6). Steps 6–13 of the PROCEDURE explain how to cast a single ray from origin to surface using this method.

### Using the length information of the rays

Casting rays to the surface of the structure assigns a length to each ray that can be used to quantify different aspects of the structure. We demonstrate two applications to cellular structures that use different aspects of the information returned by Rayburst: (A) using a 2D core to estimate diameters in tubular branching structures; (B) using a 3D core to estimate volumes and surface areas of star-convex (a subset  $X$  of  $\mathcal{R}^n$  is *star convex* if there exists an  $x_0$  in  $X$  such that the line segment from  $x_0$  to any point in  $X$  is fully contained in  $X$ ) globular structures.

#### (A) Analysis of tubular structures using 2D Rayburst

Neurons are composed of axonal and dendritic trees, whose basic element is a tubular branch section. Standard software packages for neuronal morphometry such as L-Measure<sup>21</sup>, 3DMA<sup>22</sup> and NeuroLucida (MicroBrightField) and compartment modeling packages such as NEURON<sup>23</sup> and GENESIS<sup>24</sup> represent neuronal branches as generalized cylinders, that is, as a chain of nodes with a diameter specified at each node. To extract such a representation from digital images, the structure must first be reduced to a collection of connected nodes along the center of each branch segment. This results in the medial axis or skeleton of the structure and can be obtained through a variety of methods<sup>14,16,19,25–27</sup>. To represent the 3D shape, the diameter at each node must be estimated. In earlier implementations, we used the 3D Rayburst core to estimate node diameters by computing the median lower band diameter from the ray lengths<sup>19</sup>. Validation studies against precalibrated model branching structures demonstrated that this provides a highly accurate estimate of branch diameter, irrespective of degree of taper or number of branch points (see ref. 19 for further details). In this protocol, we demonstrate an efficient 2D adaptation of this method that is faster and can eliminate the need for costly deconvolution.

For data acquired by LSM, the point spread function of the microscope can distort the apparent thickness of branches significantly along the direction of the optic axis. Although this can be largely compensated by deconvolution techniques, even the best of these leave residual smear along the optic axis (usually the  $Z$  axis of the data). In cortical and hippocampal neurons, the cross-section of dendritic branches can be assumed, from electron microscopy data in mammalian brains, to be approximately circular<sup>28</sup>. In such cases, and whenever radial measures are presumed approximately symmetric in the  $X$ ,  $Y$  and  $Z$  directions, a 2D Rayburst in the  $XY$  plane at each node is insensitive to residual  $Z$  axis smear, yielding a reliable estimate of branch diameter regardless of the orientation of the branch within the image stack. **Figure 3** demonstrates this principle, showing a 2D Rayburst (brown rays) on the cylindrical

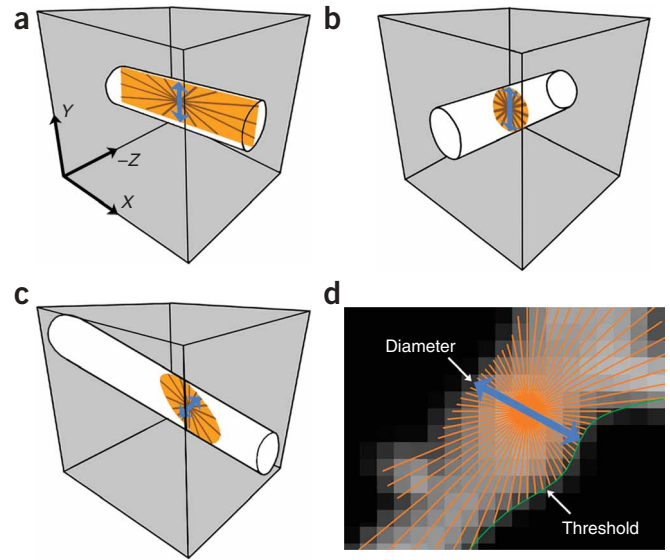


**Figure 3** | Dendritic branch diameter estimation by 2D Rayburst, irrespective of orientation of branch within image stack. The shortest span of all cylindrical sections (shown as a blue double-headed arrow) corresponds to estimated diameter. (a) The long axis of the branch is parallel to the  $XY$  plane of images. Rayburst in the  $XY$  plane will form a rectangular cylindrical section (yellow plane with superimposed rays). (b) The long axis of the branch is perpendicular to the  $XY$  plane of images. Rayburst in the  $XY$  plane forms a circular cylindrical section (yellow circle). (c) The long axis of the branch is oriented obliquely with respect to the  $XY$  plane of image stack. Rayburst in the  $XY$  plane forms an elliptical cylindrical section (yellow ellipse). (d) 2D Rayburst rendered onto confocal data. The rays cast from the sampling core are shown in gold with the one chosen as the diameter shown in blue. The subvoxel accuracy of the threshold is clearly visible when overlaid as a green line intersecting the end points of the rays.

sections (shown in gold) of a cylinder with the long axis oriented in three different ways: (i) parallel to the image plane (**Fig. 3a**); (ii) orthogonal to the image plane (**Fig. 3b**); and (iii) obliquely within the image stack (**Fig. 3c**). In each case, the shortest span (blue double-headed arrow) is of the same width and corresponds to the diameter of the cylinder.

Steps 14A(i–iv) of the PROCEDURE describe how to estimate the local diameter using the 2D Rayburst core. By varying the number of rays and reducing the distance between nodes, this information can be used to reconstruct even highly varicose dendritic branches or axons with irregular swellings. This computation can be optimized to avoid extending all rays to completion; as soon as the pair with the shortest span reaches the surface, the computation may be halted and this pair used to estimate the diameter. For data with highly irregular edges, taking the median over several adjacent rays to compute the span will increase the robustness of the estimate.

Quantitative validation tests of the 2D Rayburst diameter estimate were performed using a high-resolution simulated tubular structure of predefined diameter, in each of the three orientations shown in **Figure 3a–c**. The maximum percentage errors in the estimated diameters were 0.92, 0.71 and 1.15% for the cylinder orientations in **Figure 3a,b** and **c**, respectively. When the same simulated data were subsampled to a resolution comparable with typical LSM images discussed in this protocol, the maximum percentage errors were 2.05, 0.62 and 2.55% for the orientations shown in **Figure 3a,b** and **c**, respectively.

**(B) Analysis of complex volumetric shapes using 3D Rayburst**

An example of application of the 3D Rayburst core is estimation of the volume and surface area of a star-convex globular structure such as a dendritic spine (Figs. 4, 5a,b) or a more complex structure such as an amyloid plaque in a mouse model of Alzheimer disease (Fig. 5c,d) or other pathological processes such as tumors or vascular abnormalities. Before casting the rays, the sampling core can be visualized as a geosphere of unit radius. As the vectors are cast through the voxels of the object, the geosphere is conceptually stretched and fitted to match the true exterior manifold of the structure (Figs. 4b, 5d). The triangles on the surface of the geosphere are stored as indices into the array of vectors so that, despite their shape after sampling, the three vertices of any triangle are trivial to obtain.

**Computation of surface area and volume.** Each triangle on the geodesic sphere can be considered to be the base of a three-sided pyramid with the apex at the origin of the sampling core (Fig. 4b). Consider triangle *ABC* outlined in red in Figure 4b. This triangle forms the base of a pyramid *ABCO*, with apex at the origin of the Rayburst (*O*). For each triangle, *i*, on the surface of the sample structure, the normal, *N<sub>i</sub>*, to triangle *i* is given by the cross-product of any two sides:

$$\vec{N}_i = (\vec{B}_i - \vec{A}_i) \times (\vec{C}_i - \vec{A}_i). \tag{10}$$

The surface area of triangle *i*, *SA<sub>i</sub>*, is given by

$$SA_i = \frac{1}{2} \|\vec{N}_i\|. \tag{11}$$

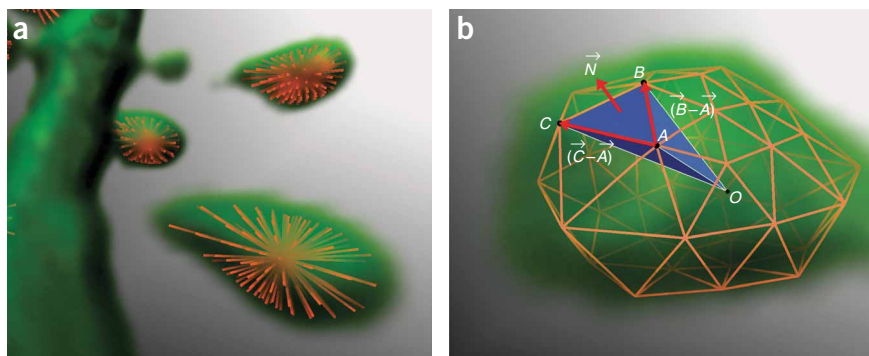


**Figure 4** | Estimation of volume and surface area of a dendritic spine using Rayburst. (a) Rayburst run from the center of mass inside each spine. (b) 3D rendering of the triangular surface mesh resulting from a low-*N* Rayburst run from the center of mass of a spine (*O*). For illustrative purposes, one of the resulting pyramids used to compute volume and surface area has been highlighted in blue. The points {*A,B,C*} are the vertices of the pyramid base whereas the vector *N* is the normal as computed by the cross-product of the vectors (*B* - *A*) and (*C* - *A*). The sum of the volumes and surface areas of all pyramids gives the total volume and surface area achieved by this Rayburst.

The volume of the *i*th pyramid is given by one-third of the surface area of the base multiplied by the height of the pyramid:

$$V_i = \frac{1}{3} SA_i \left| \frac{\vec{N}_i \cdot (\vec{A}_i - \vec{O})}{\|\vec{N}_i\|} \right|. \tag{12}$$

Or, substituting equation (11) into equation (12),

$$V_i = \frac{1}{6} \|\vec{N}_i \cdot (\vec{A}_i - \vec{O})\|. \tag{13}$$

The total volume of the structure can be computed as the sum of the volumes of these pyramids. Similarly, the surface area is computed as the sum of the areas of the bases.

**Adaptive selection of number of rays**

In applications of either 2D or 3D Rayburst, the optimum number of rays may be automatically selected at run time to achieve a specified accuracy or “critical tolerance.” For 2D Rayburst, this tolerance refers to the relative change with successive iterations in the cross-sectional area of cylindrical sections in Figure 3. For 3D Rayburst, the tolerance refers to the relative change in computed volume with successive mesh refinements. Rather than compute volume or cross-sectional area at each successive iteration, we have devised a test for detecting convergence to the optimal number of rays, based on midpoint displacement (see PROCEDURE). When the estimated tolerance computed from the data is less than the predetermined

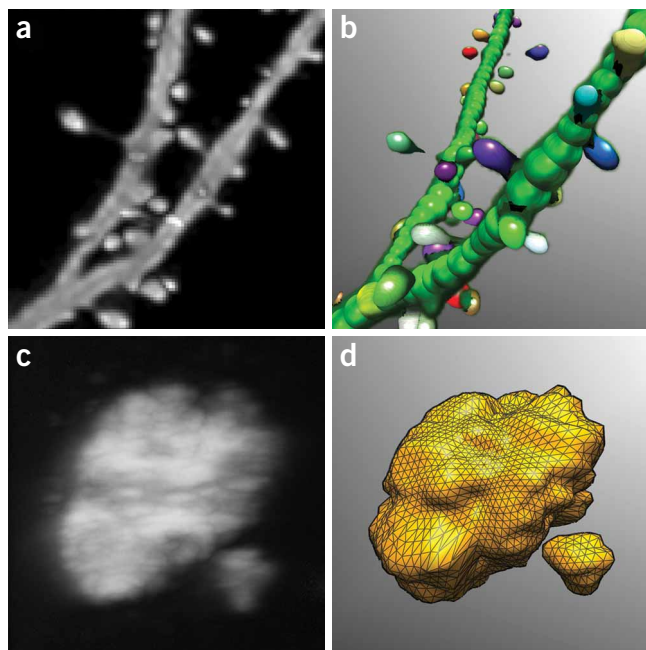


**Figure 5** | Application of Rayburst to reconstruction of a spiny dendritic branch from a layer III pyramidal neuron from prefrontal area 46 in a rhesus monkey (a,b), and a thioflavine S-labeled amyloid plaque from a Tg2576 mouse (c,d). (a) Maximal projection of the spiny dendrite. (b) Digital representation of the dendrites as a chain of nodes with associated diameters, represented as green balls along the branch. The model is superimposed on a translucent green volume rendering of the branch to illustrate the goodness of fit of model to data. Multicolored spines of various shapes are reconstructed with high-resolution surface meshes, which approximate the true spine shapes in the maximal projections (a) and volume rendered data (b) very closely. (c) Maximal projection from CLSM images of amyloid plaque. (d) Medium-resolution surface mesh reproduces complex shape and surface irregularity of the plaque with good fidelity. Greater resolution of surface irregularity can be achieved by increasing the number of rays in the Rayburst.

critical tolerance, we can assume that the number of rays is optimal for the specified accuracy level. As each iteration shares a proportion of its rays with the previous iteration, these earlier rays need not be recast, resulting in a measurable speedup of the adaptive procedure.

#### Minimum data requirements for application of Rayburst sampling

- (i) *Class of cellular morphologies to which Rayburst applies:* Although strict geometric convexity of reconstructed objects is not required, objects reconstructed by a single Rayburst must be star convex, that is, each point on the surface of the object should be accessible by a Rayburst from an interior point of origin.
- (ii) *Levels of imaging noise to which Rayburst is robust:* Depending on the quality of the data, image processing may be a prerequisite for the application of Rayburst. Unfiltered shot noise from the CCD camera can reduce the signal-to-noise ratio (SNR)<sup>29</sup> of LSM images sufficiently to affect the accuracy of Rayburst's estimates of surface area or volume. If data are extremely noisy, these estimates can be significantly improved by a simple blurring filter to reduce high-frequency noise.

The robustness of the algorithm to varying amounts of imaging noise was evaluated by generating a sample data set comprising a full-intensity sphere against a zero-intensity background, at a very high resolution (sphere diameter = 500 voxels), to allow accurate

estimation of the reference volume by voxel counting. The data set was then subsampled to 1/10 of the resolution in each direction to obtain a more realistic intensity distribution around the surface of the sphere. Noisy data sets of varying SNR values were then generated by adding Gaussian noise of specified variance to the reference data set. Rayburst was run inside each data set and a percentage error was computed based on the reference volume. To evaluate the improvement in performance when noisy data are filtered, each data set was blurred by averaging each voxel in the data set with its 26 immediate neighbors ( $3 \times 3 \times 3$  convolution kernel of equal weights) and a new Rayburst volume was computed.

The percent error in the volume estimated by Rayburst was around  $-1\%$  for an SNR of 5.54 dB and around  $-5\%$  for an SNR of 4.81 dB. When the SNR was reduced to 1.43 dB, the percent error increased to  $-37\%$ . Applying the blurring filter described above to the 1.43 dB SNR data set improved the SNR to 5.73 dB and the percent error to  $-0.17\%$ . For an extremely noisy data set with an SNR of  $-4.65$  dB, the blurring filter improved the SNR to  $-0.55$  dB and the percentage error improved from  $-98.56\%$  to under  $1\%$  after filtering. This improvement is mostly due to a reduction of below-threshold voxels in the interior of the structure by the blurring process. For structures that are much larger than the convolution kernel used for blurring, Rayburst will perform better on the blurred data than on unfiltered data of the same SNR.

## MATERIALS EQUIPMENT

- All tests reported in this protocol were performed on an Intel Pentium M 1.2 GHz PC with 1.0 GB of RAM running Windows XP Professional
- The ANSI C source code for our implementation of the Rayburst sampling algorithm with adaptive selection of number of rays can be downloaded from our website at <http://www.mssm.edu/cnic/tools.html>. This code was compiled for test purposes using the freely available Microsoft Visual C++ Toolkit 2003
- Image deconvolution for all applications described in this protocol was performed using Autodeblur (Media Cybernetics)
- Deconvolutions were performed on an SGI Onyx 3400 with eight R14K 600 MHz CPUs and 16 GB of RAM running Irix 6.5 as well as on an Intel Xeon-based PC, running at 2.2 GHz with 2.0 GB of RAM running Microsoft Windows 2000

## REAGENT SETUP

(See **Boxes 1** and **2** for further details)

- Tissue slices containing fluorescent cells, vascular networks, stained plaques or other structures of interest should be prepared for confocal or multiphoton laser scanning microscopy (CLSM and MPLSM)
- ▲ **CRITICAL** For reconstruction of large cellular structures such as pyramidal neurons from the hippocampus or neocortex, thick sections are desirable to maximize capture of large dendritic trees. The optimal section size will depend on the application for which it is intended; in particular, there is a trade-off between maximal section size (necessary to capture entire dendritic arbors of large neurons) and slice viability/cell visibility if sections are required for *in vitro* electrophysiology before labeling, or manual cell loading in fixed tissue (see **Boxes 1** and **2** for details).
- The combined constraints of manually loading neurons close to the surface of a tissue block to ensure visibility (see Cell loading techniques in **Box 1**) and the restricted working distance of approximately  $100 \mu\text{m}$  for high n.a.

lenses of the CLSM system, however, limit the Z extent of these neurons (see Imaging techniques in **Boxes 1** and **2**). This can create artifactual truncation of the dendritic tree in the Z direction. To minimize such truncation, we attempt to load neurons as deeply as possible, at depths of  $\sim 200 \mu\text{m}$  in  $400\text{-}\mu\text{m}$ -thick tissue blocks, to capture the Z extent of the dendritic tree more completely. Using longer working distance lenses of MPLSM, deep tissue blocks scanned to depths of  $200 \mu\text{m}$  from either surface can be imaged, allowing entire cells to be reconstructed from overlapping tiles<sup>30</sup>. These deep-loading and MPLSM imaging techniques are described by Rodriguez *et al.*<sup>30</sup> and summarized in **Box 1**. Axonal arbors can extend many times the length of the dendritic tree and will not be captured entirely within typical tissue sections used for slice electrophysiology or for visually guided cell loading. ▲ **CRITICAL** As with any technique to label or fill neurons *in vitro*, *in vivo* or in post-mortem materials, the issue of complete filling and ultimately of adequate recovery is a crucial one that needs to be carefully addressed. We are well aware that fine branches may not be as efficiently loaded as larger ones, and that some branches may be difficult to recover during imaging as a function of the depth within the thickness of the tissue. In addition, some branches can be cut at the surface of the slice. Issues of abnormally cut dendrites can be addressed in a variety of ways (see, e.g., Wu *et al.*<sup>31</sup>). It has been our practice to set relatively stringent criteria to retain neurons in morphometric studies. Entry into the analysis required that neurons (1) lie within the layer or region of interest as defined by cytoarchitectural characteristics (which can be verified on adjacent materials stained with cresyl violet or by staining the slice with DAPI before performing cell loading), (2) exhibit complete filling of the dendritic tree, evidenced by well-defined endings and (3) display intact primary, secondary and tertiary branches<sup>31,32</sup>. Cases where fluorescent dye is seen diffusing out of the cell body or dendrites usually indicate poor preservation of a cell's integrity or inadequate fixation of the specimen, and such cells are rejected.

## PROCEDURE

### Stepwise procedure for generating a 3D sampling core from a geodesic sphere

**1** | We demonstrate this recursive procedure using an octahedron as the basis for our geodesic sphere (**Fig. 1**). We first define a right-handed cartesian coordinate system  $[X,Y,Z]$  with positive directions of the axes pointing rightward, upward and forward, respectively, according to a right-handed screw rule, as illustrated in **Figure 1a**.



## BOX 1 | TISSUE PREPARATION, MICROSCOPY METHODS AND IMAGING TECHNIQUES

The following sections describe methods used to label and image the spiny dendritic branches and amyloid beta plaques shown in **Figures 4** and **5** of this protocol, and to reconstruct the apical and basal dendritic trees of pyramidal neurons from multiple-tiled image stacks using confocal and multiphoton laser scanning microscopy (CLSM and MPLSM), also described by Rodriguez *et al.*<sup>30</sup> and Wearne *et al.*<sup>19</sup>.

### Tissue preparation and microscopy methods

**Animals:** The brains of long-tailed macaque monkeys (*Macaca fascicularis*), Tg2576 mice older than 12 months, and wild-type littermates, were used for cell loading and 3D reconstruction of spiny dendritic branches and entire pyramidal neurons shown in this protocol and in our previous studies that have been used for 3D neuronal reconstructions<sup>19,30,35,36</sup>. All animal protocols were approved by the Animal Care and Use Committee at Mount Sinai School of Medicine. For reconstruction of amyloid plaques from human tissue, blocks from the prefrontal cortex (Brodmann's area 9) and from the hippocampus were obtained at autopsy, after verification of consent, from patients with Alzheimer disease (78–85 years old, post-mortem interval 3–8 h) through the Mount Sinai School of Medicine Alzheimer's Disease Research Center Brain Bank. One hemisphere was fixed in 4% (wt/vol) paraformaldehyde for 3–4 weeks and subsequently sampled for quantitative histopathology<sup>37</sup>.

**Tissue preparation.** For imaging and reconstruction of single neurons, spiny dendrites and multineuron networks, mice were perfused transcardially with a mixture of 4% paraformaldehyde and 0.125% glutaraldehyde in phosphate buffer (phosphate-buffered saline (PBS); pH 7.4) for 10 min. Monkeys were perfused intracardially as described previously<sup>36,38,39</sup>. In brief, the monkeys were deeply anesthetized with ketamine hydrochloride (25 mg kg<sup>-1</sup>) and pentobarbital sodium (20–35 mg kg<sup>-1</sup>, i.v.), intubated and mechanically ventilated. The chest was opened to expose the heart, and 1.5 ml of 0.1% sodium nitrite was injected into the left ventricle. The descending aorta was clamped and the monkeys were perfused transcardially with cold 1% paraformaldehyde in PBS for 1 min and then for 12 min with cold 4% paraformaldehyde and 0.125% glutaraldehyde in PBS. Brains were carefully removed from the skull, hemisected under a dissecting microscope and sectioned on a vibratome (Leica) at 200  $\mu$ m for mice<sup>19</sup> and at 400  $\mu$ m for monkeys<sup>35,36</sup>. For imaging of amyloid beta plaques in transgenic mice, senile plaques were first visualized in thick sections with 0.01% thioflavine S, and sections were coverslipped with SlowFade (Molecular Probes). This permits visualization of the loaded neurons in the context of amyloid plaque distribution in Tg2576 mice and reveals the possible effects of amyloid on the integrity of dendrites and spines. Materials from human brains were cut at 300  $\mu$ m on a vibratome and the sections were stained with thioflavine S for senile plaque visualization as above. For monkeys, after hemisection, 4–5 mm thick blocks of tissue from prefrontal cortex area 46 were taken perpendicular to the axis of the principal sulcus and processed as described above and by Duan *et al.*<sup>35,36</sup>.

**Autofluorescence quenching.** The autofluorescent component of an image due to lipofuscin may be removed by spectral imaging and linear unmixing, as described in "Imaging techniques," below. Moreover, the autofluorescence of human sections due to lipofuscin can be quenched by treatment of the mounted sections in 1% Sudan Black B in 70% alcohol, rehydrated and coverslipped<sup>40</sup>. This provides an efficient removal of bleed-through autofluorescence in case high levels of lipofuscin are present in human materials and in the oldest mice.

**Cell loading in fixed slices with Lucifer Yellow.** For intracellular injection, thick sections were incubated with 4,6-diamidino-2-phenylindole (DAPI; Sigma), a fluorescent nucleic acid stain, for at least 5 min, to reveal the cytoarchitecture under UV excitation. Sections were mounted on nitrocellulose filter paper, immersed in phosphate-buffered saline (pH 7.4) and visualized under epifluorescence. Using DAPI staining as a guide, neurons are impaled with sharp micropipettes and loaded with 5% Lucifer Yellow (Molecular Probes) in distilled H<sub>2</sub>O under a direct current of 3–8 nA for 10–12 min or until the dye fills distal processes and no further loading is observed<sup>19,35,36</sup>. Alternatively, to prevent artifacts due to artificial sectioning of dendrites at either surface of the tissue slab, which occurs in most cases for average-sized pyramidal neurons loaded within the first 100  $\mu$ m of the surface, cells can be loaded blindly deep in the tissue, aiming with the micromanipulator at depths of about 200  $\mu$ m. This permits a fuller loading of all dendritic branches. After neuronal labeling, sections were fixed again in 4% paraformaldehyde and 0.125% glutaraldehyde in PBS for 4 h at 4 °C, washed and stored in PBS. Sections were then mounted on uncoated slides, coverslipped in PermaFluor and loaded neurons were visualized by CLSM. Neurons loaded deeply in the tissue must be imaged using a long working distance lens and MPLSM, using techniques described by Rodriguez *et al.*<sup>30</sup>

### Imaging techniques

**Laser scanning microscopy (confocal and multiphoton).** Tissue sections were examined using a BioRad Radiance 2000 multiphoton laser-scanning microscopy (MPLSM) system (Hercules) equipped with a Coherent Mira 900F Ti:sapphire laser and a Kr/Ar (488, 568 nm) laser. Tissue sections were also examined using a Zeiss LSM 510 META confocal laser scanning microscope (Jena) equipped with Ar (488 nm) and HeNe (543, 633 nm) lasers and/or a Leica TCS-SP (UV) confocal laser scanning microscope, equipped with Ar (488 nm), Kr (568 nm) and HeNe (633 nm) lasers. For MPLSM, fluorescence from labeled neurons was imaged by using the Ti:sapphire laser (tuned to 860 nm for Lucifer Yellow) and a UPlanApo/IR 60X (1.2 n.a., 0.25 mm WD) water immersion objective lens. Serial optical sections (1,024  $\times$  1,024 pixels; pixel dimensions = 0.2  $\times$  0.2  $\mu$ m) were collected through focus at 0.2  $\mu$ m intervals. For higher resolution imaging, a UPlanApo  $\times$ 100/1.35 n.a. objective (WD 0.1 mm) was used on the BioRad system in the multi-photon mode (i.e., with the Ti:sapphire laser) and/or the single-photon (confocal) mode (with the 488 nm line of the Kr/Ar laser). Single photon (confocal) imaging was also made on a Leica TCS-SP (UV) CLSM using a  $\times$ 100, 1.4 n.a. PlanApo lens and the 488 nm line of an Ar laser or on a Zeiss LSM 510 META confocal laser scanning using a  $\times$ 63, 1.4 n.a. PlanApo lens and the 488 nm line of an Ar laser. Serial optical sections (1,024  $\times$  1,024 pixels with pixel dimensions = 0.18  $\times$  0.18  $\mu$ m (BioRad) or 0.1  $\times$  0.1  $\mu$ m (Zeiss or Leica)) were collected through focus at 0.1  $\mu$ m intervals and correction for signal attenuation will be performed as described above. Collected data are saved to disk as BioRad pic files or stacks of TIFF images (Leica and Zeiss) and processed independently of each other before volume integration and reconstruction with the VIAS-NeuronStudio system<sup>30</sup>.

**Spectral imaging and linear unmixing.** For the amyloid plaque reconstructed in **Figure 5c,d** of this protocol, thioflavine S-labeled slides were imaged on a Zeiss LSM 510 META confocal laser scanning microscope equipped with a  $\times$ 63, 1.4 n.a. oil immersion PlanApo objective lens. The META detector was used to generate spectral signatures (over a 240 nm range) for thioflavine S-labeled plaques and for lipofuscin

**BOX 1 | CONTINUED**

autofluorescence in unlabeled sections. Lambda scanning was performed for thioflavine S-labeled sections and advanced linear unmixing (using the LSM 510 software) was used to separate the spectrally overlapping fluorescence of the thioflavine S-labeled senile plaques and the lipofuscin autofluorescence. The lipofuscin component of the image was removed, leaving the thioflavine S components for 3D reconstruction and analysis using the Rayburst sampling algorithm (see Wearne *et al.*<sup>19</sup>, Fig. 12 and p. 676, for further details).

- 2| Place the octahedron with its center at the origin of the coordinate system and normalize each vertex so that it lies on the surface of a unit sphere (**Fig. 1a**).
- 3| Subdivide each triangular face into four smaller triangles, and normalize each new vertex, pushing it onto the surface of the unit sphere (**Fig. 1b**).
- 4| Repeat Step 3 until the desired number of faces is achieved (**Fig. 1c,d**).
- 5| Define a set of unit length rays from the origin to each vertex of the resulting polyhedron (**Fig. 1e**). This becomes the 3D Rayburst core (**Fig. 1f**). Vertex connectivity is saved for use in surface area and volume calculations.

**Stepwise procedure for casting rays through volume (for each ray)**

- 6| Compute  $i, j$  and  $k$  according to equations (1–3).
- 7| Compute the times of exit  $\{t_x, t_y, t_z\}$  for each face according to equations (7–9).
- 8| Select  $t_{\min}$ , which identifies face of exit.
- 9| Substitute  $t = t_{\min}$  into equations (4–6) to determine exit location  $[x_f, y_f, z_f]$ .
- 10| Perform bilinear interpolation over the face of exit to determine intensity value at exit location ( $I_f$ ), and compare to threshold value,  $I_T$ . If  $I_f < I_T$ , go to Step 12.
- 11| Update origin of ray as  $x_0 = x_f, y_0 = y_f, z_0 = z_f$  (**Fig. 2a**) and repeat the process from Step 6.
- 12| Linearly interpolate along the ray between the last two values of  $I_f$  to determine the location of threshold,  $[x_T, y_T, z_T]$ .
- 13| Convert  $x_T, y_T, z_T$  and the origin of the Rayburst to actual physical dimensions by multiplying by the corresponding voxel dimension. The distance to the surface is given by the distance between these two locations.

**Stepwise procedure for using the length information of the rays**

- 14| You can now use either (A) 2D Rayburst or (B) 3D Rayburst.
- (A) Estimating the diameter using 2D Rayburst at a given node along the medial axis of the structure**
- (i) Place the 2D Rayburst core with origin on the node.
  - (ii) Cast all rays in the core according to Steps 6–13.
  - (iii) Once all rays reach the surface of the structure, pair each ray with its diametric opposite. The sum of these two distances gives the local wall-to-wall distance or *span*.
  - (iv) Select the pair with the minimum span as an estimate of the local diameter of the structure (blue diameters, **Fig. 3**).

**BOX 2 | IMAGING**

Serial optical sections should be collected through focus at intervals sufficient to allow adequate deconvolution during post-processing, and saved to disk.

To optimize resolution of the 3D structure recovered by Rayburst sampling, we recommend using the highest available numerical aperture (n.a.), the highest pixel resolution in the image plane and Z-step intervals sufficient to approximate cubic voxels as closely as possible<sup>19,30</sup>. In recent tests to assess the minimum image quality necessary to recover accurate neuronal tree geometry, we found that a minimum of  $\times 60$  magnification (1.4 n.a.) with 8-bit grayscale range and voxel sizes of approximately  $0.2 \times 0.2 \times 0.2 \mu\text{m}$  (field size  $1,024 \times 1,024$ ) was required for adequate automated reconstruction of both branching topology and spine morphology of typical layer III neocortical pyramidal neurons, without significant manual intervention<sup>19</sup>. Nonetheless, even using a  $\times 40$  (0.6 n.a.) objective lens with 8-bit grayscale range, we have successfully reconstructed the dendritic trees of such neurons, provided that disconnected dendrites were visually reconnected during a final manual tree-editing phase (see Wearne *et al.*<sup>19</sup> for details).

For optimal 3D shape analysis, adequate deconvolution is important, using either an experimentally measured point spread function or a theoretical point spread function calculated from the data, as is used in blind deconvolution. All data shown in this protocol were processed with the montaged blind deconvolution system AutoDeblur (Media Cybernetics), which we find produces excellent results for data obtained by CLSM or MPLSM.



**(B) Computing surface areas and volumes using 3D Rayburst**

- (i) Place the 3D Rayburst core inside the structure at the center of mass.
- (ii) Cast all rays in the core according to Steps 6–13.
- (iii) Compute Volume,  $V_i$ , and surface area,  $SA_i$ , of each pyramid,  $i$ , formed by the rays (**Fig. 4b**), according to equations (10–13).
- (iv) Compute total volume,  $V$ , and surface area,  $SA$ , of the structure by summing over all volumes and surface areas of individual pyramids,  $i = 1, \dots, n$ .

**Stepwise procedure for adaptive selection of number of rays**

**15|** Define critical tolerance,  $tol_{(crit)}$ , and initial discretization (**Fig. 1a**).

**16|** Run Rayburst at current discretization.

**17|** Compute center point for each mesh triangle,  $i$ , or perimeter segment in the case of a 2D core, at the current discretization level of  $n$  triangles;  $d_{C_i}$  = distance from origin to center point of triangle  $i$ .

**18|** Cast ray from origin in the direction of center point to surface;  $d_{S_i}$  = distance from origin to surface.

**19|** Compute estimated tolerance,

$$tol_{(est)} = \frac{\sum_{i=1}^n |d_{S_i} - d_{C_i}|}{\sum_{i=1}^n d_{C_i}};$$

If  $tol_{(est)} > tol_{(crit)}$ , refine mesh to next level of discretization (**Fig. 1b**); cast new rays only (note that rays from all previous iterations are kept, but not re-cast at Step 18); repeat from Step 17.

**20|** Otherwise compute volume, surface area or diameter of the structure at this iteration.

● **TIMING**

For applications to 3D neuronal reconstruction described in this protocol, the time-consuming tissue preparation, imaging and deconvolution procedures are the bottlenecks. Once images are available, the shape analysis procedures using Rayburst are comparatively rapid, with representative times described as follows.

Timing tests for 2D and 3D Rayburst were measured on the Intel Pentium 1.2 GHz (see EQUIPMENT) and are representative of the performance of that system. Execution time for 2D Rayburst sampling is proportional to the number of voxels in the cross-sectional area of the structure being measured. As a representative example, 1,000 samples were taken at various locations inside a typically imaged dendritic segment (12 voxels in diameter) using a convergence tolerance setting of 1%. This resulted in a total running time of 15.8 s for the 1,000 samples, or 15.8 ms per sample. The execution time for 3D Rayburst sampling is proportional to the number of voxels in the volume of the structure being measured. As a representative example, a single Rayburst sample was run inside a typical amyloid plaque imaged with CLSM (**Fig. 5c,d**) containing a structure of roughly 8 million voxel units in volume. Using a convergence tolerance setting of 1%, the total running time was measured at 5.4 s.

? **TROUBLESHOOTING**

Troubleshooting advice can be found in **Table 1**.

**TABLE 1 |** Troubleshooting table.

Problem	Possible reason	Solution
Part of a structure is missing in the reconstruction	Structure is not star-convex	Run Rayburst from multiple origins inside the object
Surface mesh does not follow contours of the structure well	Too few rays in Rayburst core	Run Rayburst with increasing number of rays until the computed surface area converges
Some rays do not reach the surface of the structure	Noisy data	Adjust deconvolution parameters to reduce noise; filter to remove noise during preprocessing
	Structure has internal “holes”	Flood-fill structure before running Rayburst
Rays and surface mesh either underestimate or overestimate the surface of the object	Incorrect threshold value selected	Re-run thresholding procedure until surface mesh matches the surface of the object
Artificial stretching of structure along the Z axis	Inadequate deconvolution	Check deconvolution parameters are correctly matched to microscopy parameters



ANTICIPATED RESULTS

For reconstruction and analysis of spiny neurons, a digital representation of the dendritic tree can be output in standard neuroanatomical format<sup>33</sup> as a chain of nodes with associated diameters and connectivity parameters. This format can reproduce dendritic trees and spine morphology to arbitrarily high resolution by increasing the numbers of nodes in the tree and rays in the Rayburst. **Figure 5a,b** shows an example of a reconstructed spiny dendritic branch with superimposed spines. Variability in the dendritic diameter apparent in the maximal projection of the raw images (**Fig. 5a**) is captured well by a moderate discretization of nodes along the medial axis and associated diameters represented by green spheres (**Fig. 5b**). Spine morphology is also well captured by a high-*N* Rayburst surface mesh (colored spines, **Fig. 5b**). In practice, we have found that a relatively high-*N* Rayburst (~2,500 rays for a typical dendritic spine imaged with CLSM) does not compromise execution speed and gives excellent results, as it tends to fit the convex structure precisely while allowing rays to penetrate finer substructures such as the necks of spines. **Figure 5c,d** shows a reconstructed amyloid plaque from a Tg2576 mouse carrying the Swedish mutation of the amyloid precursor protein<sup>34</sup>, labeled with thioflavine S and imaged on a Zeiss LSM 510 META microscope in confocal mode (see Wearne *et al.*<sup>19</sup> for details). The highly irregular surface of the plaque seen in the maximal projection (**Fig. 5c**) is well reproduced by the two triangulated surfaces resulting from Rayburst cores run separately inside the large (upper) and smaller (lower) plaque fragments (**Fig. 5d**).

Other potential applications of the Rayburst technique include different imaging modalities such as serial section electron microscopy, widefield imaging, live two-photon images or magnetic resonance angiography. The only constraint on potential applications is that the images can be adequately segmented (see section “Minimum data requirements for application of Rayburst”).

The Rayburst sampling algorithm presented in this protocol is a versatile 3D shape analysis technique for LSM images that uses interpolation of the original grayscale data to estimate distance measurements linearly within a voxel. Rayburst can be implemented as an automated shape analysis system for multiple applications in biology and other fields where precise structural quantification is critical, at scales ranging from submicrometric to arbitrarily large. By providing accurate 3D morphometry of complex histological structures, these techniques will enable multiscale biophysical modeling studies capable of testing potential mechanisms by which morphologic alterations give rise to the functional deficits that characterize disease states.

**ACKNOWLEDGMENTS** This work was supported by NIH grants from NIMH, NIDCD, NIA and NCR. The authors thank colleagues in the Wearne and Hof laboratories for their participation.

**COMPETING INTERESTS STATEMENT** The authors declare that they have no competing financial interests.

Published online at <http://www.natureprotocols.com>  
 Reprints and permissions information is available online at <http://npg.nature.com/reprintsandpermissions>

1. Vetter, P., Roth, A. & Häusser, M. Propagation of action potentials in dendrites depends on dendritic morphology. *J. Neurophysiol.* **85**, 926–937 (2001).
2. Euler, T. & Denk, W. Dendritic processing. *Curr. Opin. Neurobiol.* **11**, 415–422 (2001).
3. Stuart, G., Spruston, N. & Häusser, M. *Dendrites* (Oxford University Press, Oxford, 1999).
4. Rothnie, P., Kabaso, D., Hof, P.R., Henry, B.I. & Wearne, S.L. Functionally relevant measures of spatial complexity in neuronal dendritic arbors. *J. Theor. Biol.* **238**, 506–526 (2004).
5. Mainen, Z.F. & Sejnowski, T.J. Influence of dendritic structure on firing pattern in model neocortical neurons. *Nature* **382**, 363–366 (1996).
6. Krichmar, J.L., Nasuto, S.J., Scorcioni, R., Washington, S.D. & Ascoli, G.A. Effects of dendritic morphology on CA3 pyramidal cell electrophysiology: a simulation study. *Brain Res.* **941**, 11–28 (2002).
7. Ascoli, G.A. Passive dendritic integration heavily affects spiking dynamics of recurrent networks. *Neural Networks.* **16**, 657–663 (2003).
8. Häusser, M. & Mel, B.W. Dendrites: bug or feature? *Curr. Opin. Neurobiol.* **13**, 372–383 (2003).
9. Bloom, F.E., Young, W.G., Nimchinsky, E.A., Hof, P.R. & Morrison, J.H. Neuronal vulnerability and informatics in human disease. in *Neuroinformatics—An Overview of the Human Brain Project* (eds. Koslow, S.H. & Huerta, M.F.) 83–123 (Mahwah, Lawrence Erlbaum, 1997).
10. Streekstra, G.J., Smeulders, A.W.M. & van den Boomgaard, R. Scale dependent differential geometry for the measurement of center line and diameter in 3D curvilinear structures. in *6th European Conference on Computer Vision 2000* (Dublin, Ireland, 2000).
11. Streekstra, G.J. & van Pelt, J. Analysis of tubular structures in three-dimensional confocal images. *Network Comput. Neural Systems* **13**, 381–395 (2002).
12. Dima, A., Scholz, M. & Obermayer, K. Semi-automatic quality determination of 3D confocal microscope scans of neuronal cells denoised by 3D-wavelet-shrinkage. In: H.H. Szu, ed., *Wavelet Applications VI—Proceedings of the SPIE*, **3723**, 446–457 (1999).
13. Messerli, M. *NeuronTracer Reference Manual V. 1.0#1–33* (Zurich, Bitplane AG, 2000).
14. Schmitt, S., Evers, J.F., Duch, C., Scholz, M. & Obermayer, K. New methods for the computer-assisted 3-D reconstruction of neurons from confocal image stacks. *NeuroImage* **23**, 1283–1298 (2004).
15. He, W. *et al.* Automated three-dimensional tracing of neurons in confocal and brightfield images. *Microsc. Microanal.* **9**, 296–310 (2003).
16. Al-Kofahi, K.A. *et al.* Rapid automated three-dimensional tracing of neurons from confocal image stacks. *IEEE Trans. Inform. Tech. Biomed.* **6**, 171–187 (2003).
17. van Pelt, J., van Ooyen, A. & Uylings, H.B.M. The need for integrating neuronal morphology databases and computational environments in exploring neuronal structure and function. *Anat. Embryol.* **204**, 255–265 (2001).
18. Ashby, N. & Brittin, W.E. Thomson’s problem. *Am. J. Phys.* **54**, 776–777 (1986).
19. Wearne, S.L. *et al.* New techniques for imaging, digitization and analysis of three-dimensional neuronal morphology on multiple scales. *Neuroscience* **136**, 661–680 (2005).
20. Hill, S. Trilinear interpolation. in *Graphics Gems IV* (ed. Heckbert, P.S.) 521–525 (Academic Press, San Diego, 1994).
21. Scorcioni, R. & Ascoli, G.A. Algorithmic extraction of morphological statistics from electronic archives of neuroanatomy. in *IWANN 2001, Lecture Notes in Computer Science* (eds. Mira, J. & Prieto, A.) 30–37 (Springer-Verlag, Berlin, Heidelberg, 2001).
22. Weaver, C.M., Hof, P.R., Wearne, S.L. & Lindquist, W.B. Automated algorithms for multiscale morphometry of neuronal dendrites. *Neural Comput.* **16**, 1353–1383 (2004).
23. Hines, M.L. The NEURON simulation program. in *Neural Network Simulation Environments* (ed. Skrzypek, J.) 147–163 (Kluwer, Norwell, MA, 1994).
24. Bower, J.M. & Beeman, D. *The Book of Genesis: Exploring Realistic Neural Systems with the General Neural Simulation System* 2nd edn. (Springer-Verlag, New York, NY, 1998).



25. Blum, H. A transformation for extracting new descriptors of shape. in *Models for the Perception of Speech and Visual Form* (ed. Wathen-Dunn, W.) 362–380 (MIT Press Cambridge, MA, 1967).
26. Koh, I.Y.Y., Lindquist, W.B., Zito, K., Nimchinsky, E.A. & Svoboda, K. An image analysis algorithm for the fine structure of neuronal dendrites. *Neural Comput.* **14**, 1283–1310 (2002).
27. Borgefors, G., Nystrom, I. & Sanniti Di Baja, G. Computing skeletons in three dimensions. *Pattern Recognition* **32**, 1225–1236 (1999).
28. Peters, A., Palay, S.L. & Webster, H.D. *The Fine Structure of the Nervous System* (Oxford University Press, New York, 1991).
29. Jain, A.K. *Fundamentals of Digital Image Processing* (Prentice-Hall, Englewood Cliffs, NJ, 1989).
30. Rodriguez, A. *et al.* Automated reconstruction of 3D neuronal morphology from laser scanning microscopy images. *Methods Companion Methods Enzymol.* **30**, 94–105 (2003).
31. Wu, C.-C., Reilly, J.F., Young, W.G., Morrison, J.H. & Bloom, F.E. High-throughput morphometric analysis of individual neurons. *Cereb. Cortex* **14**, 543–554 (2004).
32. Hao, J. *et al.* Estrogen alters spine number and morphology in prefrontal cortex of aged female rhesus monkeys. *J. Neurosci.* **26**, 2571–2578 (2006).
33. Cannon, R.C., Turner, D.A., Pyapali, G.K. & Wheal, H.V. An on-line archive of reconstructed hippocampal neurons. *J. Neurosci. Methods* **84**, 49–54 (1998).
34. Hsiao, K. *et al.* Correlative memory deficits, A $\beta$  elevation, and amyloid plaques in transgenic mice. *Science* **274**, 99–102 (1996).
35. Duan, H., Wearne, S.L., Morrison, J.H. & Hof, P.R. Quantitative analysis of the dendritic morphology of corticocortical projection neurons in the macaque monkey association cortex. *Neuroscience* **114**, 349–359 (2002).
36. Duan, H. *et al.* Age-related morphologic alterations in dendrites and spine densities of corticocortically projecting neurons in macaque monkeys. *Cereb. Cortex* **13**, 950–961 (2003).
37. Perl, D.P. *et al.* Practical approaches to stereology in the setting of aging and disease-related brain banks. *J. Chem. Neuroanat.* **20**, 7–19 (2000).
38. Hof, P.R., Nimchinsky, E.A. & Morrison, J.H. Neurochemical phenotype of corticocortical connections in the macaque monkey: quantitative analysis of a subset of neurofilament protein-immunoreactive projection neurons in frontal, parietal, temporal and cingulate cortices. *J. Comp. Neurol.* **362**, 109–133 (1995).
39. Nimchinsky, E.A., Hof, P.R., Young, W.G. & Morrison, J.H. Neurochemical, morphologic and laminar characterization of cortical projection neurons in the cingulate motor areas of the macaque monkey. *J. Comp. Neurol.* **374**, 136–160 (1996).
40. Romijn, H.J. *et al.* Double immunolabeling of neuropeptides in the human hypothalamus as analyzed by confocal laser scanning fluorescence microscopy. *J. Histochem. Cytochem.* **47**, 229–235 (1999).

